Composites Science and Technology

The analysis of the ultimate blast failure modes in fibre metal laminates

E. Sitnikova [a], Z.W. Guan [b, c, *], W.J. Cantwell [d]

[a] *Faculty of Engineering, University of Nottingham, University Park, Nottingham, NG7 2RD, UK*
[b] *School of Engineering, University of Liverpool, Brownlow Street, Liverpool, L69 3GQ, UK*
[c] *School of Mechanical Engineering, Chengdu University, Chengdu, 610106, PR China*
[d] *Department of Aerospace Engineering, Khalifa University of Science, Technology and Research (KUSTAR), Abu Dhabi, United Arab Emirates*

ARTICLE INFO

ABSTRACT

Finite element modelling has been applied to simulate various failure modes in fibre metal laminate (FML) panels under localized high intensity blast loading. A relatively simple material model, based on continuum damage mechanics, has been proposed to describe the constitutive response of the composite material in the FMLs. Simulations of the blast response of FMLs with various stacking configurations has been carried out, capturing both perforation and non-perforation failure modes. Blast loading was modelled by a pressure function applied on the front face of the FML panel. The definition of the pressure function accounts for both the temporal as well as the spatial distribution of the blast. The capability of the models has been assessed by comparing the predictions associated with both low and high intensity blast cases with published experimental data. Good qualitative and quantitative agreement has been observed for lay-ups with similar proportions of aluminium and composite. It is believed that the models can be employed for use in parametric studies that would facilitate the adoption of FMLs in wider engineering design.

1. Introduction

A fibre-metal laminate (FML) is a type of sandwich structure consisting of alternating layers of metal and fibre-reinforced composite. The particular interest in using these hybrid materials is linked to their attractive properties, such as high strength/weight ratio, cost-effectiveness, an ability to tailor material properties, and good fatigue, impact and corrosion resistance. These attributes make FMLs suitable for a range aerospace applications [1].

As impact damage is a relatively common failure type in aircraft structures, the response of FMLs to such form of dynamic loading has been extensively studied, both numerically and experimentally [2]. Numerous experimental studies have been carried out to investigate the influence of the constituents on the impact properties of FMLs. Vlot [3] showed that the puncture energies glass laminate aluminium reinforced epoxy (GLARE), could be higher than those of aluminium sheets of the same thickness. Abdullah

and Cantwell [4] conducted impact tests on FMLs made with two different aluminium alloys, and showed that the perforation resistance was higher for FMLs based on a stronger alloy. Yaghoubi and Liaw [5] noted that interfacial debonding was influenced by the composite stacking sequence of the FML.

For applications in the design of the aerospace structures, FMLs should also possess an adequate blast resistance to meet the necessary safety requirements. A number of numerical and experimental studies have conducted to investigate various aspects of the blast response of FMLs. In particular, Langdon et al. [6,7] undertook an experimental study to investigate the effects of localized blast loading on both thin and thick FML panels. The authors presented a systematic account of the large variety of failure scenarios observed following the tests. In particular, the tests showed that in thick panels with a high proportion of composite material, one of the principal failure mechanisms was extensive debonding of the back face aluminium layer, with the debonded area increasing with increasing impulse. Numerical modelling of the response of GLARE panels to the blast loading has been undertaken by Mohamed et al. [8] and Kotzakolios et al. [9], who used different finite element codes in their investigations. Predictions of the mid-point deflection and global deformation, as well as damage in the panels, were

* Corresponding author. School of Engineering, University of Liverpool, Brownlow Street, Liverpool, L69 3GQ, UK.
   E-mail address: zguan@liverpool.ac.uk (Z.W. Guan).

compared with those obtained experimentally, showing a reasonable level of agreement between the two. These studies, however, were concerned only with the assessment of the deformation and the damage modes in the FMLs for cases where perforation of the panels did not occur.

A critical review of published work on numerical and analytical modelling of the impact response of FMLs was carried out by Morinière et al. [10]. They stated that conducting impact tests on FMLs is very time-consuming and the experimental results are typically scattered, meaning that a large number of tests are required to obtain statistically significant data. Therefore, in order to carry out systematic studies on the impact response of FMLs, reliable modelling techniques need to be developed and applied to complement the associated experimental studies.

One of the commonly employed approaches for the numerical analysis of FML failure is through finite element (FE) modelling using commercially-available software packages. In these types of models, each of the FML constituent materials is assigned an appropriate material behaviour [8,9,11]. However, modelling the constitutive response of the composite is not fully established, due to the complexity of damage initiation/evolution, strain-rate dependence and failure mechanisms in these materials. Because of this, simplifying assumptions are often made when describing the material behaviour of the composite materials in FMLs, such as treating the thin woven composite as an isotropic layer within the plane [12]. Many composite failure models are based on a plane-stress state material response, in accordance with the assumptions of Classical Laminate Theory. This can be a limitation in modelling through-thickness impact damage [8], when high compressive stresses occur in the material. Gama and Gillespie [13] proposed a constitutive model that accounts for a strain-rate dependence and damage evolution in both unidirectional and woven composites under a 3D stress state. In terms of modelling the rate-dependent material response, the model has certain limitations, such as the rate-dependency of the material strengths being prescribed via a single rate scaling coefficient.

The definition of the blast loading event is yet another issue when modelling the blast response of FMLs. In many finite element software codes, models for the explicit definition of the explosive are often available. In some studies on blast failure of FMLs [9,14], those models were directly applied to define the blast loading. Though this provides a reasonable representation of blast loading, the main drawback of these types of model are the high associated computational costs, since the explicit definition of the explosive also requires definition of the fluid-structure interaction. Specifically, Soutis et al. [14] simulated the blast failure of a GLARE panel using two finite element models. In the first model, blast charge was modelled explicitly, while in the second model it was prescribed via a simpler, but more computationally effective algorithm, where blast load was defined by a pressure function applied on the surface of the target. The study showed that the latter approach can reduce the CPU time by a factor of 10.

Modelling blast loading via a pressure function applied on the surface of the target has also been adopted in some other studies investigating blast failure in FMLs [8,11,15], where reasonable agreement between the observed and simulated responses of the FML panels were achieved.

In the current paper, blast damage and associated failure are simulated in FML panels based on various lay-ups subjected to a variety of loading scenarios. A relatively simple continuum mechanics based model is proposed to define the constitutive behaviour of the composite. The formulation is applicable for composites based on a plain weave, an architecture that provides a superior impact or shock resistance in structures than unidirectional reinforcements [16]. Comparisons with experiments [6,7] are

carried out to assess the predictive capability of the models. In contrast to previous modelling efforts on this subject [11,15,17], both perforation and non-perforation modes of failure are captured, yielding an insight into blast failure in FLMs. Furthermore, the current composite model incorporates the most common aspects of the dynamic failure process in fibre reinforced composites, namely, a 3D constitutive behaviour, damage evolution and rate-dependent characteristics.

2. Modelling the constitutive response of FML panels

In this work, a range of finite element models of FML panels with various stacking sequences were created and analysed. The geometry, constituent materials and stacking sequences of these panels match those used in previous experimental studies [6,7].

The tested panels were based on various stacking sequences of aluminium alloy 2024-O and woven glass fibre reinforced polypropylene (GFPP) composite plies. The stacking sequences of the panels are referred to using the same AXTYZ notation as was suggested in Refs. [6,7]. Here, the character "A″ denotes the aluminium constituent, and "T″ refers to Twintex™, which is the tradename of the GFPP composite constituent. Character X signifies the number of aluminium sheets, $Y = X - 1$ defines the number of composite layers, with Z being the number of composite plies in each layer.

The mechanical response of each of the FML constituent materials, i.e. the aluminium, composite and adhesive layer, was prescribed via a relevant material model. Deformation and failure in the aluminium layers were modelled using Johnson-Cook plasticity and failure criteria available in Abaqus [18]. The constitutive response of the layers of adhesive was defined using a traction-separation description of cohesive elements, which is also available in Abaqus. A brief summary of the modelling approaches used is given in the Appendix. However, the composite material model available in Abaqus is unsuitable for the analysis of the problem considered here, as it was developed for studying failure in laminated composites based on the unidirectional laminaes and plane-stress conditions. Therefore, in order to describe blast failure in the composite, a 3D material model, incorporating both damage evolution and strain-rate effects, was developed and implemented into the VUMAT subroutine.

2.1. Constitutive equations for glass fibre reinforced composite

The macroscopic constitutive behaviour of the woven composite material is considered as being orthotropic. Therefore, the compliance matrix can be written as follows:

$$S^0 = \begin{bmatrix} 1/E_1^0 & -\nu_{21}^0/E_2^0 & -\nu_{31}^0/E_3^0 & 0 & 0 & 0 \\ -\nu_{12}^0/E_1^0 & 1/E_2^0 & -\nu_{32}^0/E_3^0 & 0 & 0 & 0 \\ -\nu_{13}^0/E_1^0 & -\nu_{23}^0/E_2^0 & 1/E_3^0 & 0 & 0 & 0 \\ 0 & 0 & 0 & 1/G_{12}^0 & 0 & 0 \\ 0 & 0 & 0 & 0 & 1/G_{23}^0 & 0 \\ 0 & 0 & 0 & 0 & 0 & 1/G_{13}^0 \end{bmatrix},$$

(1)

where E_i^0, G_{ij}^0 and ν_{ij}^0 with $i,j=1...3$ are the elastic constants and Poisson's ratios of the undamaged material.

The symmetry of the compliance matrix and consequently the stiffness matrix, is ensured by imposing the following symmetry conditions:

$$\frac{\nu_{ij}^0}{E_i^0} = \frac{\nu_{ji}^0}{E_j^0}, \quad i,j = 1..3 \tag{2}$$

The material properties of the virgin composite material are given in Table 1. The process of modelling damage is based on a continuum damage mechanics approach, first introduced by Kachanov [19], who proposed the use of a scalar quantity, called a damage variable, for quantifying the accumulation of dissipated damage in isotropic materials. As damage grows, the damage variable increases from zero to unity, where zero describes the virgin material, and unity defines complete material failure.

For the case of an anisotropic material, damage accumulation can vary in different directions, and in order to account for such damage non-uniformity, a damage tensor, instead of a scalar variable, is commonly used. Here the explicit form of the damage tensor is chosen to be as follows:

$$D = diag\left((1-d_1)^{-1}, (1-d_2)^{-1}, (1-d_{3c})^{-1}, (1-d_{12})^{-1}, \right.$$
$$\left. (1-d_2)^{-1}, (1-d_1)^{-1}\right) \tag{3}$$

where the terms d_i are damage variables, namely, d_1 and d_2 correspond to failure in the warp and weft fibre directions, respectively, d_{3c} describes through-the-thickness composite crushing failure, and $d_{12} = \max(d_1, d_2)$ refers to in-plane shear failure. The variables d_1 and d_2 take different values in tension and compression and are therefore defined as:

$$d_1 = 1 - (1-d_{1t})(1-d_{1c}), \quad d_2 = 1 - (1-d_{2t})(1-d_{2c}), \tag{4}$$

where the subscripts "t" and "c" denote tensile and compressive failure, respectively.

In order to account for the influence of damage on the stress state, the effective stresses $\widehat{\sigma}$ are defined, which are related to the true stresses σ as follows:

$$\widehat{\sigma} = D\sigma, \sigma = [\sigma_{11}, \sigma_{22}, \sigma_{33}, \sigma_{12}, \sigma_{23}, \sigma_{31}]^T, \widehat{\sigma}$$
$$= [\widehat{\sigma}_{11}, \widehat{\sigma}_{22}, \widehat{\sigma}_{33}, \widehat{\sigma}_{12}, \widehat{\sigma}_{23}, \widehat{\sigma}_{31}]^T \tag{5}$$

With the onset of damage, the strain in the material is defined as:

$$\varepsilon = S^0 \widehat{\sigma} = S^0 D\sigma = S\sigma, \tag{6}$$

where S is a compliance tensor for the damaged composite. Defined in this way, S will have the same form as S^0 in Eq. (1) with the elastic constants for the undamaged material replaced with their "damaged" counterparts using the expressions given below:

$$E_1 = E_1^0(1-d_1), \quad E_2 = E_2^0(1-d_2), \quad E_3 = E_3^0(1-d_{3c}),$$
$$G_{12} = G_{12}^0(1-d_{12}), \quad G_{23} = G_{23}^0(1-d_2), \quad G_{13} = G_{13}^0(1-d_1),$$
$$\nu_{12} = \nu_{12}^0(1-d_1), \quad \nu_{13} = \nu_{13}^0(1-d_1), \quad \nu_{23} = \nu_{23}^0(1-d_2)$$
$$\nu_{21} = \nu_{21}^0(1-d_2), \quad \nu_{31} = \nu_{31}^0(1-d_{3c}), \quad \nu_{32} = \nu_{32}^0(1-d_{3c}). \tag{7}$$

The expressions for the Poisson's ratios of the damaged material in Eq. (7) are obtained by assuming that the symmetry of the compliance tensor is maintained during all of the stages of damage. Hence, the symmetry conditions in Eq. (2) should also hold for the

Table 1
Composite material parameters [11].

ρ (kg/m³)	E_1, E_2 (GPa)	E_3 (GPa)	ν_{12}	ν_{23}, ν_{13}	G_{12} (GPa)	G_{23}, G_{13} (GPa)
1800	13	4.8	0.1	0.3	1.72	1.69

damaged material.

Finally, the stiffness matrix of the damaged material, C, can be obtained by inverting the compliance matrix S, and therefore, the stress-strain dependence of the damaged material becomes:

$$\sigma = S^{-1}\varepsilon = C\varepsilon \tag{8}$$

Eqs. (7) and (8) form the damage representation of the current problem. This formulation needs to be supplemented with damage initiation criteria and damage evolution laws in order to fully describe the failure processes in the composite.

2.2. Damage initiation criteria

The damage initiation criteria are a set of conditions which, once satisfied, trigger the evolution of damage. Five different failure conditions are considered in order to account for various damage modes. Tensile-shear failure criteria, similar to the fibre failure criteria [20] were used to describe the damage initiation conditions in the warp and weft fibre directions, as follows:

$$f_{1t} = \left(\frac{\widehat{\sigma}_{11}}{\sigma_{1t}^r}\right)^2 + \zeta\left(\frac{\widehat{\sigma}_{12}}{\sigma_{12}^r}\right)^2 + \left(\frac{\widehat{\sigma}_{31}}{\sigma_{31}^r}\right)^2 - 1 \geq 0, \quad \sigma_{11} > 0, \tag{9}$$

$$f_{2t} = \left(\frac{\widehat{\sigma}_{22}}{\sigma_{2t}^r}\right)^2 + \zeta\left(\frac{\widehat{\sigma}_{12}}{\sigma_{12}^r}\right)^2 + \left(\frac{\widehat{\sigma}_{23}}{\sigma_{23}^r}\right)^2 - 1 \geq 0, \quad \sigma_{22} > 0, \tag{10}$$

where the coefficient $\zeta = 0.1$ controls the contribution of the shear component. Under shear loading, the material exhibits a plastic-like response, which becomes non-linear at low values of stress, while ultimate failure occurs at high values of strain [22]. Since shear nonlinearity is not incorporated in the present model, to prevent premature predictions of failure, due to the contribution of shear component, its value was scaled down.

The remaining three damage modes define damage under compression in the warp, weft and through-the-thickness direction. These are described by the maximum stress criteria as:

$$f_{ic} = \left(\frac{\widehat{\sigma}_{ii}}{\sigma_{ic}^r}\right)^2 - 1 \geq 0, \quad \sigma_{ii} < 0, \quad i = 1, 2, 3 \tag{11}$$

The properties σ_{ab}^r, $ab = 1t, 1c, 2t, 2c, 3c, 12, 23, 31$ in Eqs. (9–11) are the damage initiation stresses. In order to represent the dynamic material response, the strain-rate dependency was assigned to them as follows [13,23]:

$$\sigma^r(\dot{\varepsilon}) = \sigma^s\left(1 + R\ln\frac{|\dot{\varepsilon}_{ii}|}{\dot{\varepsilon}_0}\right), \tag{12}$$

where σ^s is a static strength and R is a strain-rate constant. Their values are given in Table 2. The same reference strain-rate value, $\dot{\varepsilon}_0 = 1\,s^{-1}$, has been used for all failure modes. It is worth noting that the in-plane strain-rate scaling factors, R_i, as specified in Table 2, were determined experimentally by Brown et al. [22] for this particular composite material, Twintex. The out-of-plane scaling factors were not available, hence, as a conservative measure, the out-of-plane strengths were assigned with a very low strain rate sensitivity, in order to avoid over-estimating the blast resistance of the FML panels.

2.3. Damage evolution

To model the evolution of the damage variable, the formulation proposed by Iannucci [24] was adapted. In Ref. [24] damage

Table 2
Composite material strength values and strain-rate coefficients.

	$\sigma^r_{1t}(\dot{\varepsilon}_{11}), \sigma^r_{2t}(\dot{\varepsilon}_{22})$	$\sigma^r_{1c}(\dot{\varepsilon}_{11}), \sigma^r_{2c}(\dot{\varepsilon}_{22})$	$\sigma^r_{3c}(\dot{\varepsilon}_{33})$	$\sigma^r_{12}(\dot{\varepsilon}_{12})$	$\sigma^r_{13}(\dot{\varepsilon}_{13}), \sigma^r_{23}(\dot{\varepsilon}_{23})$
σ^s, MPa [11,21]	300	200	300	40	120
R [22]	0.089	0.181	0.005	−0.061	0.005

variable evolution was defined in an incremental form, whereas in the present study it was further simplified to allow for the direct calculation of the total value the of damage variable at each time increment. At the onset of failure, the damage variable for the corresponding failure mode was calculated as follows:

$$d_{it} = \alpha_1 f_{it}, \quad \text{if } f_{it} \geq 0, \, \Delta\varepsilon_{ii} > 0, \quad i = 1, 2$$
$$d_{ic} = \alpha_2 f_{ic}, \quad \text{if } f_{ic} \geq 0, \, \Delta\varepsilon_{ii} < 0, \quad i = 1, 2 \qquad (13)$$
$$d_{3c} = \alpha_3 f_{3t}, \quad \text{if } f_{3t} \geq 0, \, \Delta\varepsilon_{33} < 0,$$

Parameters α_1 - α_3 in Eq. (13) govern the rate of growth of the damage variable. The values of the parameters were determined via a parametric study, where the values of α_1 - α_3 were varied, whilst the remaining parameters were kept fixed. The predictions were compared with the deformation and failure modes observed experimentally. Specifically, the deformation modes in panel A2T18 at the applied impulse of $I = 6.17$ Ns, predicted with two different sets of damage coefficients, are shown in Fig. 1(a) and (b). In the first case, the values of the parameters were set to zero, assuming instant failure in each mode. As can be seen, perforation failure was predicted, which is not consistent with the behaviour observed experimentally, where the panel was not perforated. With value of the coefficient α_1, associated with in-plane tensile/shear damage of the panel, being set to 0.2, there is closer agreement between the predicted and the experimental response, however, the back face deflection was still substantially overestimated. Based on the similar analyses of a number of loading cases, the values $\alpha_1 = 0.2$, $\alpha_2 = 2.0$, $\alpha_3 = 1.0$ were determined to be appropriate for most of the cases. It is worth noting that α_i are regarded as the material properties. Therefore, their values can be different if different material system is used. In absence of the established experimental techniques for determining these properties, calibrating their values based on experimental data might be the only method available at present. However, the study conducted suggests that only a few experiments should be required to calibrate the values of α_i for any given material system.

Additional conditions on the strain increments, $\Delta\varepsilon$, were imposed in Eq. (13) in order to ensure that damage evolution takes place only at increasing absolute values of strain.

2.4. User-defined subroutine implementation and single element model predictions

The progressive failure model introduced in previous sections was implemented into the main Abaqus program, through a VUMAT subroutine. The structure of the subroutine is shown in flowchart form in Fig. 2.

For element deletion, a conservative approach has been adopted, namely, the element is considered to have failed and is removed from the mesh when a damage variable associated with any mode of damage reaches a critical value, $\omega_{max} = 0.95$. This is to avoid excessive distortion of elements caused by a stiffness reduction when complete damage is reached in one mode, which is a common problem in the explicit analysis.

To verify the implementation of the composite failure model, typical material responses were calculated based on a single element model. The plots, shown in Fig. 3(a) and (b), were obtained for uniaxial loading in the 1-direction and the through-thickness direction, respectively. The load was applied at a constant strain rate, and four such loading cases were considered. In both cases, the damage initiation stress increased with strain rate. For the in-plane tensile damage mode, at the high strain rates, a pronounced non-linear behaviour beyond damage initiation was observed, and the stress, as well as the strain, reached higher maximum values, indicating the enhanced reactive material response at the higher strain rates. This effect was less pronounced for the though-thickness damage mode, for which the strain rate scaling coefficient was lower. Also, in this case, a higher value of the parameter a_2 governing the growth of the damage variable has been used, which in turn leads to a more rapid degradation of stiffness.

3. Modelling blast loading on the FMLs panels

3.1. Finite element model of the panel

The finite element model of the panel is identical in terms of geometry to that described by Sitnikova et al. [17], formed on the basis of two earlier studies [11,15].

A quarter of the FML panel was modelled, with appropriate symmetry and boundary conditions applied, as shown in Fig. 4. In the experiments [7], the mean thickness of each panel tested was measured. During the manufacture, the thickness of the panel could not be precisely controlled, hence there were small variations in the panel thickness in each FML. Here, the same average thickness value was assumed for all the panels based on the same lay-up. The aluminium layer thickness of 0.6 mm and thermoplastic interlayer thickness of 0.05 mm (assumed) were kept constant for all of the FML lay-ups. The composite layer thickness was calculated by subtracting the total aluminium and cohesive layer thickness from the measured average panel thickness and dividing it by the number of composite layers. The calculated composite layer thickness in each FML lay-up, along with the average panel thicknesses are presented in Table 3.

A 3D constitutive behaviour was considered for all the constituent materials. Hence, 8-noded solid elements, with reduced integration (C3D8R), were used to mesh the aluminium layers and composite plies. The cohesive layers were meshed using C0H3D8
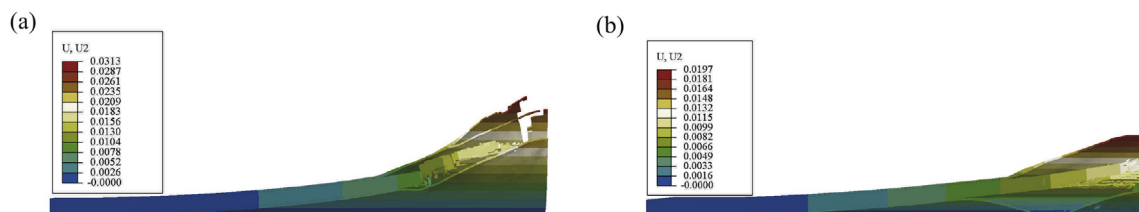
(a)

(b)

Fig. 1. Deformation of panel A2T18 at $I = 6.17$ Ns calculated using different values of damage coefficients α_1 - α_3: (a) $\alpha_1 = \alpha_2 = \alpha_3 = 0$; (b) $\alpha_1 = 0.2$, $\alpha_2 = \alpha_3 = 0$.
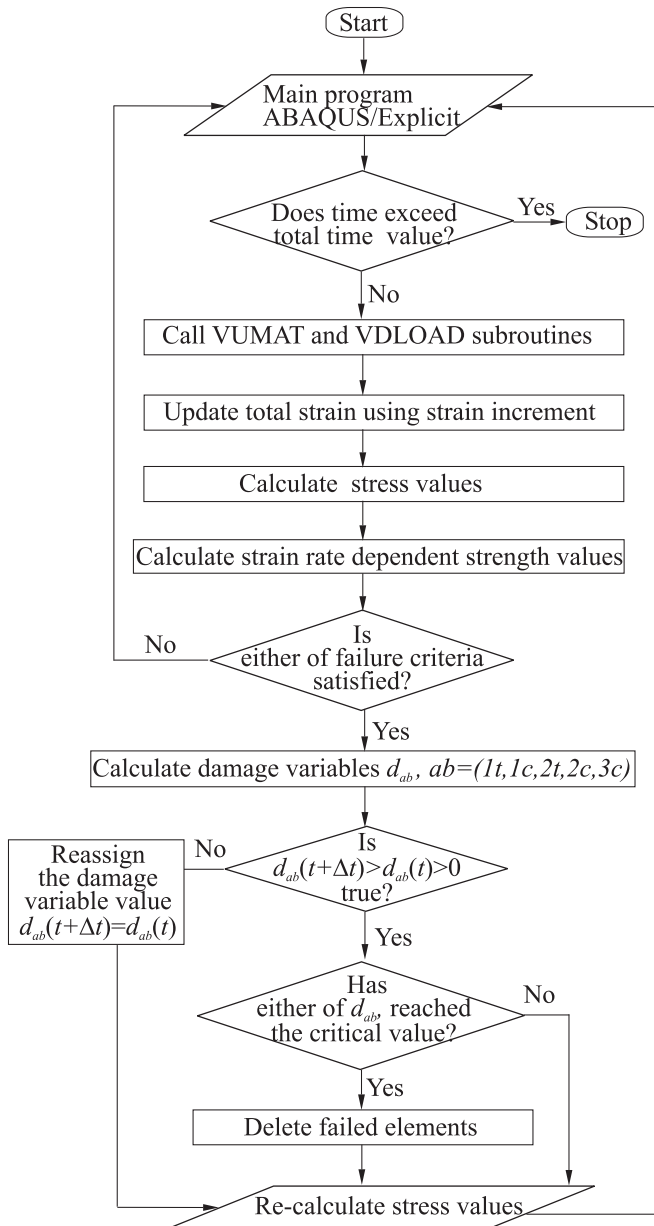
Fig. 2. Flowchart of the VUMAT subroutine for calculating the blast response of the composite material.

elements. A biased mesh was generated outside the central 60×60 mm area of the panel, where a finer mesh size of 1×1 mm was used [17]. A general contact interaction was defined on both the exterior and interior faces of the contacting composite and aluminium layers to address possible contact scenarios after the cohesive layer fails.

3.2. Modelling of the applied blast pressure

Blast loading acting on FML panels was modelled as a surface pressure applied to the front face aluminium sheet. The pressure is a function of time t and distance r from the panel centre, and its explicit expression was proposed as [11]:

$$P(r,t) = P_1(r)P_2(t) \tag{14}$$

An example of a spatial pressure distribution plot is shown in Fig. 5(a), and its explicit expression can be written as follows [11]:

$$P_1(r) = \begin{cases} P_0 & \text{if } r \leq r_0, \\ P_0 e^{-k(r-r_0)} & \text{if } r_0 < r \leq r_b, \\ 0 & \text{if } r > r_b, \end{cases} \tag{15}$$

Here $r_0 = 0.015$ m is the radius of the explosive, $k = 130$ m^{-1} is the decay constant, and $r_b = 0.1$ m is the radius of the area around the explosive, beyond which the pressure can be considered negligibly small.

The pulse-time history plot is shown in Fig. 5(b), and is expressed as

$$P_2(t) = \begin{cases} t/t_* & \text{if } t \leq t_*, \\ e^{-b(t-t_*)/t_0} & \text{if } t > t_*. \end{cases} \tag{16}$$

where $t_* = 10\ \mu s$ and $t_0 = 60\ \mu s$ are the time constants and $b = 2$ is an exponential decay parameter. The temporal distribution of blast, as proposed in Refs. [17,25] was adopted here. It was suggested in Refs. [17,25] that prior to an exponential decay, the pressure increases linearly over a short time interval. This provides a more physical representation of the blast loading process, allowing the material to react to the applied pressure, rather than provide an instant response.

Next, the total blast impulse I was calculated as

$$I = 2\pi \int_0^\infty \int_0^{r_b} rP(r,t)\, dr\, dt, \tag{17}$$

An explicit expression for calculating the pressure amplitude is obtained from Eqs. (15–17) as follows:
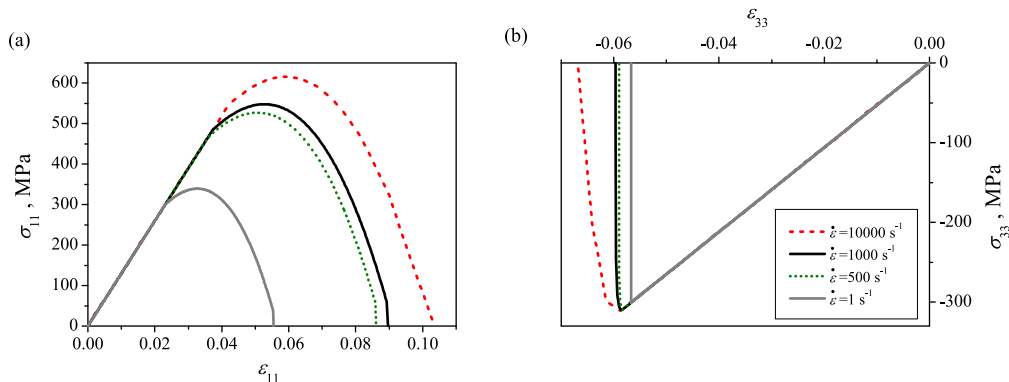

Fig. 3. Composite constitutive behaviour at different strain rates obtained for a single element FE model: (a) stress-strain curves under tension in 1-direction; (b) stress-strain curves under compression in 3-direction.
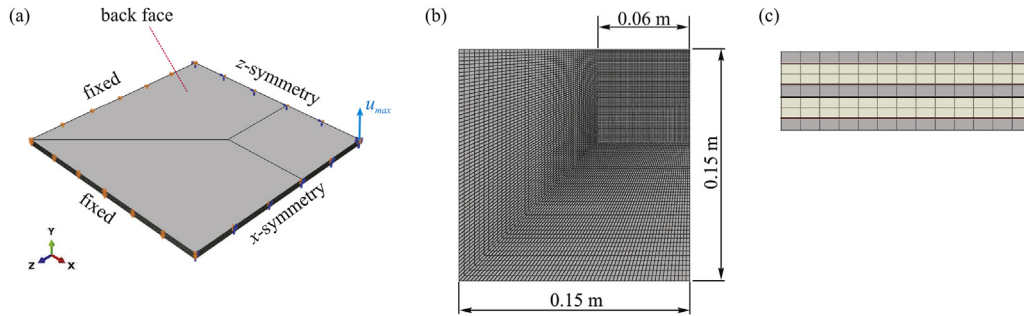
Fig. 4. FE model of A3T22 panel: (a) symmetry and boundary conditions; (b) in-plane mesh; (c) through the thickness mesh.

Table 3
Thickness of composite layers in FML lay-ups.

Lay-up	A2T12	A2T14	A2T18	A3T22	A3T24	A3T28	A4T32	A4T34	A5T42
Average panel thickness,mm	2.37	3.37	5.56	4.11	6.12	9.75	5.82	8.64	7.43
Composite layer thickness, mm	1.07	2.07	4.26	1.05	2.06	3.88	1.04	1.98	1.01

$$P_0 = \frac{I}{\pi \left(t_0 + t_*\right)\left[\frac{r_0^2}{2} + \frac{1}{k}\left(r_0 - \left(r_b + \frac{1}{k}\right)\right)e^{-k(r_b - r_0)} + \frac{1}{k}\right]} \qquad (18)$$

The magnitudes of I were measured in the experiments [6,7], for all of the loading cases. This allows for the direct calculation of the pressure amplitude, P_0, for each loading case. The loading function, as described here, was implemented through a VDLOAD user-defined subroutine.

4. Numerical results and discussion

4.1. Comparison of the failed FML panels with numerical predictions

Using the FE models described above, the blast responses associated with a number of loading cases were calculated for different FML lay-ups. To validate the accuracy of the numerical predictions, a comparison with the experimental results reported in Refs. [6,7] was carried out. In these experiments, the deformation and failure patterns in the various FML lay-ups were presented in the form of digital images of the front and back faces [7] and cross-sections through the centre of the panel [6]. Additionally, the maximum residual displacement, u_{max}, of the back face, was measured for cases where the FMLs did not fail in a perforation mode. In order to obtain the residual displacement values, the calculations were run until the time reached 0.005 s, which was sufficiently long for the panel to numerically recover from the blast.

The predicted displacement contour plots are presented alongside the experimental images, and the calculated residual displacements were compared with the measured values, in cases where such data was available. To facilitate comparisons of the deformation and failure modes, an Abaqus post-processing tool was used to reflect the quarter panels with respect to their planes of symmetry.

In Fig. 6, the calculated displacement contour plots are compared with the experimental panels for the A2T1Z configuration series. The panels contained two aluminium layers and one composite layer comprised of 2, 4 or 8 plies. For the thinnest panel, A2T12, perforation failure was predicted at $I = 10.34$ Ns, and the rupture and outward petalling around the circumference of the perforation hole was captured in both the front and back face aluminium layers. For the A2T14 panel, large global inelastic deformation of the panel was predicted for an impulse $I = 5.89$ Ns, and there is a good agreement between the measured and predicted residual back face displacements. Similarly, good agreement between the measured and calculated back face displacement was obtained for A2T18 panel at $I = 6.17$ Ns. Because of presence of a the thicker composite core, this panel is stiffer than the A2T14 panel, hence the global deflection of the panel (i.e. the global inelastic deformation of the panel) is relatively small, and the maximum back face displacement is smaller than that in the A2T14 panel. The central displacement was associated with debonding and plastic deformation of the rear face in the centre of the panel. Finally, perforation failure in the A2T18 panel was predicted at $I = 10.19$ Ns. Comparing the contour plot of this panel with that of the A2T12 panel at $I = 10.34$ Ns, it is clear that, although the applied pulses were very similar, failure in A2T18 is more localised, and the global
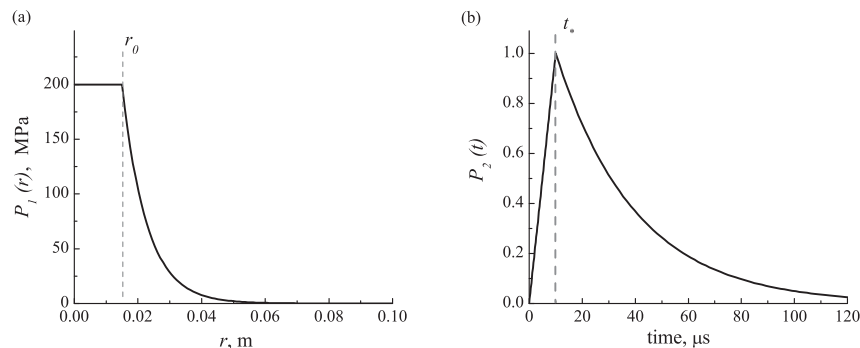

Fig. 5. Pressure pulse for $P_0 = 200$ MPa, $k = 130$ m^{-1}, $r_0 = 0.015$ m, $t_*=10$ μs and $t_0 = 60$ μs: (a) spatial pressure distribution; (b) time history.
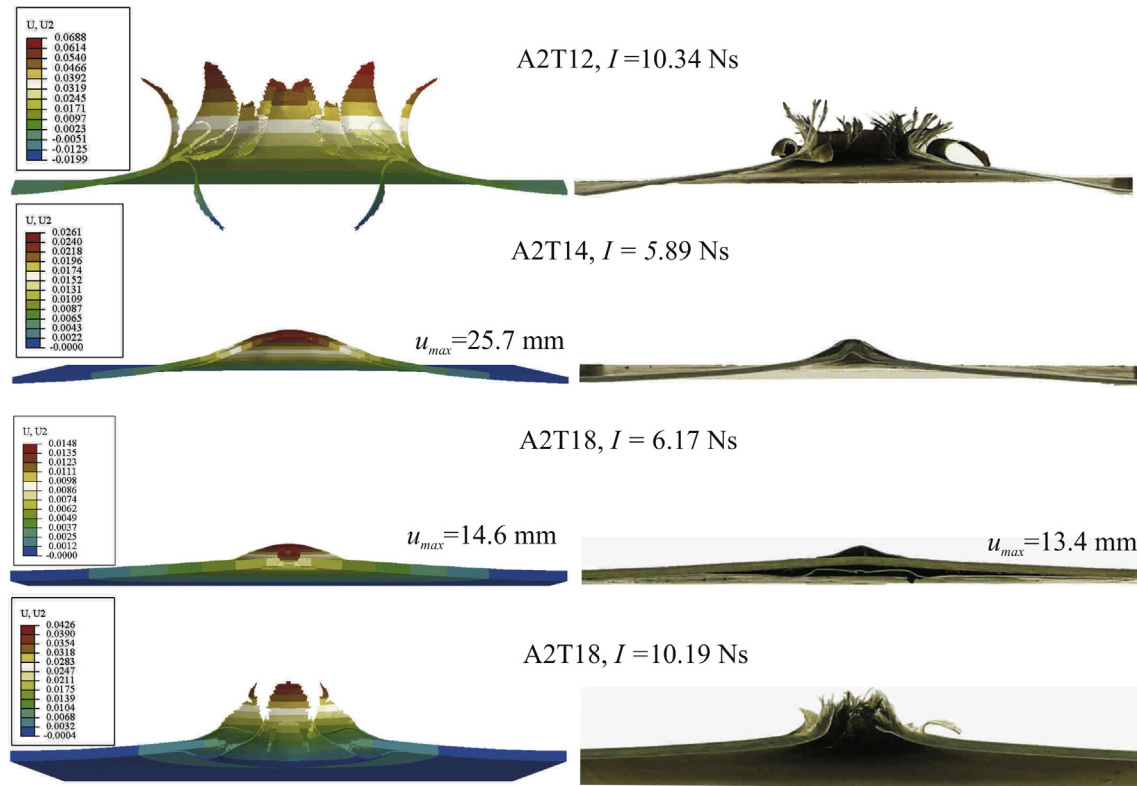
Fig. 6. Comparison of the predicted displacement contour plots with the experimental data [6] for panel lay-ups with two outer aluminium layers and a composite core of increasing thickness over a range of the blast impulses.

deflection is smaller. This suggests that the strength and the stiffness properties of the A2T18 panel are higher than those of the A2T12 FML. These simple observations, as well as the good agreement between the measured and calculated back face displacements, serve as the initial check on the validity of the FE model.

Next, contour plots of the AXTY2 panel configuration were compared with the cross-sections of the test panels, as shown in Fig. 7. These lay-ups had between 2 and 5 aluminium layers, whereas each composite layer consisted of two plies. These panels had similar proportions of aluminium and composite [7], with the aluminium weight fraction reducing from 48% in the A3T22 lay-up to 45% in the A5T42 panels. Once again, for all the loading cases considered here, good agreement between the predictions and the experimental results is evident, in terms of the calculated back face displacement, as well as the deformation and failure modes of the panels. In particular, multiple debonding between the aluminium and composite layers in the centre of the panel was captured for the A5T42 FML panel at $I = 14.7$ Ns. However, the model tends to underestimate the residual displacement as the number of the constituent layers increases, i.e. the thickness of the lay-up increases. As the weight fraction of composite in the panels increases with the panel thickness, the contribution of composite failure to the deformation and failure of the panel becomes more significant. A composite model with a conservative criterion for element deletion, as used here, is expected to provide a prediction of premature, hence overestimated, failure. It has been shown previously [17] that failure of the composite affects the deformation and damage development process in the adjacent constituent layers and consequently the entire panel. Furthermore, relation between the debonding of the back face and the deformation of composite layers has been observed in the experiments [7], where the weave orientation in the composite has shown to affect the debonding pattern on the back face. Therefore, the predicted early failure of

the composite inevitably influences prediction of the extent of back face debonding and deformation, hence the residual displacement of the back face.

This also explains the predicted premature failure of the back face aluminium layer in the A3T24 FML panel at an applied impulse of $I = 10.58$ Ns, as shown in Fig. 8, where the displacement contour plots for this FML for four loading cases are presented. In all cases, reasonable agreement between the predictions and the experimental results has been obtained for the A3T24 FML. At the same time, the model tends to overestimate the global deflection and failure threshold of this panel. Specifically, at $I = 3.76$ Ns, little global panel deflection and a small central back face debonded region occurred during the test, while the debonding was not captured in the simulations. In addition, a larger global panel deflection was predicted. At $I = 7.85$ Ns, the observed back face debonding in the centre of the panel was captured numerically. However, in the simulations, the cross-section of the debonded back face was of a rounded "dome-like" shape, while in the test panel it took a triangular form. At $I = 10.58$ Ns, a small indentation in the front face aluminium layer and a localised region of damage in the inner composite and aluminium layers were observed experimentally, while in the simulations, the predicted damaged area of the composite layers was noticeably larger. By analysing the images of the tested FML panels with a similar damage mode, it became clear that the indentation in the centre of the front face aluminium layer occurred due to the high intensity of loading applied in this area. Indeed, in the experiments, the detonator was attached to the centre of the disk of the explosive using a 1 g mass of explosive. For small charges, this can constitute up to one third of a total mass of the explosive. It is likely that this type of failure cannot be reproduced by the models used here, where a constant pressure is applied over the whole area of explosive. Finally, at $I = 16.19$ Ns the model captures the perforation failure mode, yet
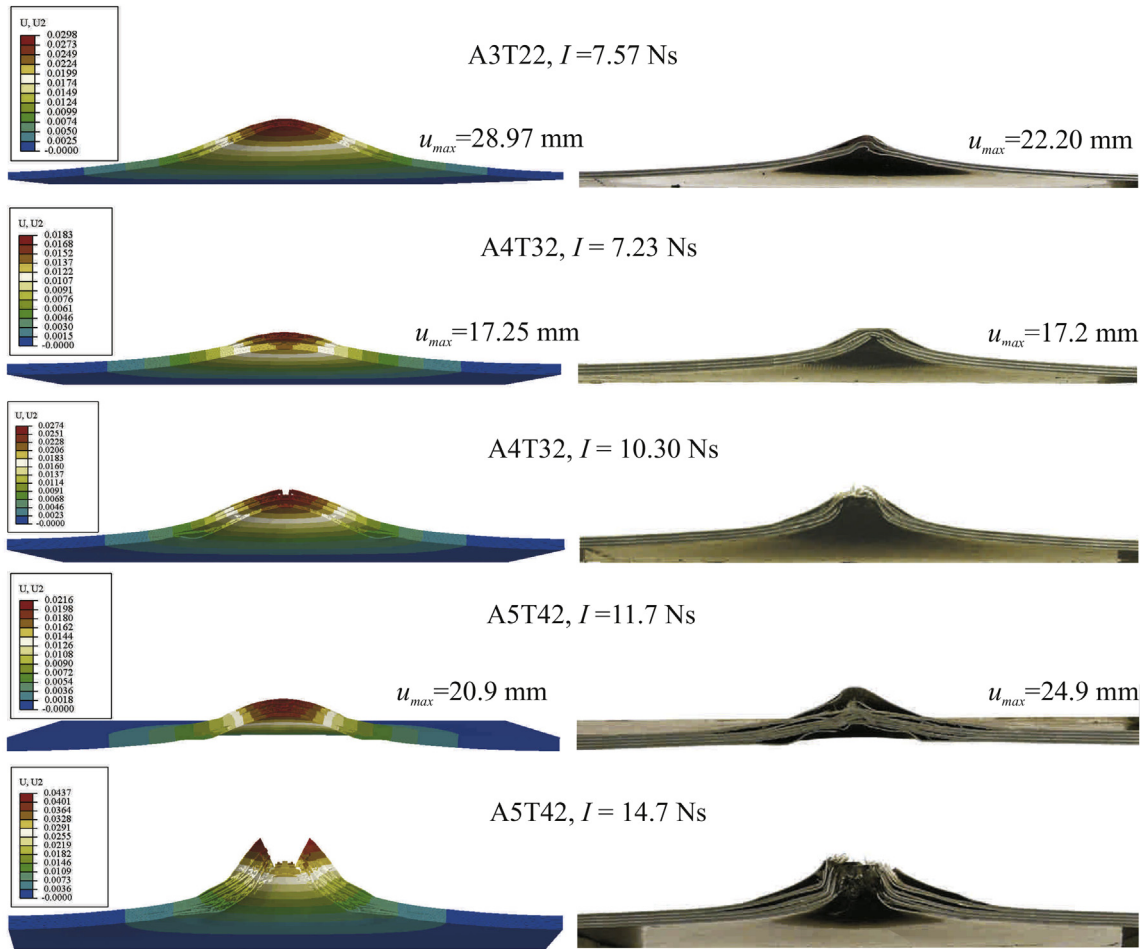
Fig. 7. Comparison of the predicted displacement contour plots with the experimentally observed deformation [6] of FML panels of A2T1Z configuration series.

overestimates the extent of failure in the centre of the panel.

Similar observations can be made when analysing the predicted failure modes in the FML lay-up A4T34, for which three loading cases were simulated, as shown in Fig. 9. In particular, at $I = 7.01$ Ns, the predicted global deflection of the panel was larger than that in the experiment. At $I = 11.84$ Ns, debonding of the back face was captured by the model, yet the debonded area was smaller than in the experiment. Once again, a rounded shape on the debonded back face was predicted, this being in contrast to the triangular shape observed experimentally. It is interesting to note that, for this loading case, a failure mode has been predicted, that has not been captured in any of the previous analyses [15,17], this being the debonding of the front face aluminium layer and the formation of a "crater-like" damage pattern, which was described in Ref. [7]. This failure mode occurred mainly in the panels with over 16 constituent layers (aluminium sheets and GFPP plies). Based on a visual inspection of the residual deformation in the panels, this effect was explained by in-plane compression and buckling of the front layers [7]. It was noted that since the global residual displacement of the front face layer was small, and the bending resistance of the thick panels is high, in-plane compression is the most likely cause for buckling of the front face layer. However, analysis of the predicted transient response of the panels suggests a different scenario of a "crater-like" front face damage formation. The transient response of the FML panel A4T34 at $I = 11.84$ Ns is presented as a series of contour plots of the in-plane stress σ_{22} in Fig. 10. At $t = 0.1$ ms (Fig. 10(a)), a localised panel deflection over the blast area occurred, where the deflections of the front and the back layer were of a

similar magnitude. As a result, stretching and plastic deformation of the aluminium sheets occurred. As the stress wave propagated towards the boundary of the plate, global panel deflection occurred, as shown in Fig. 10(b). At this point, the plastically-deformed front and back face aluminium layers are debonded from the adjacent composite layers. The maximum panel deflection is achieved at $t = 0.7$ ms (Fig. 10(c)), after which the panel began to recover its elastic deformation. During the recovery phase, the composite layers "forced" the front face aluminium sheet to buckle, as shown in Fig. 10(d).

Finally, two loading cases were simulated for the A3T28 FML lay-up, which are shown in Fig. 11. The "crater-like" front face damage pattern was predicted in both cases, and an analysis of the transient responses confirmed that it developed in the same way as described above. The model captured the back face layer debonding at $I = 12.43$ Ns, and perforation failure with the outward petalling of the back face aluminium layer for a blast impulse $I = 18.99$ Ns. This lay-up has the highest volume fraction of composite amongst all the panel configurations considered here. Therefore, the effects of the premature composite failure are the most pronounced for this lay-up. In particular, for a blast impulse $I = 18.99$ Ns the predicted size of the perforation hole in the centre of the panel was overestimated as compared to that in the test panel. Similarly, the over-prediction of the perforation hole size also occurred in panels A3T24 at $I = 16.19$ Ns (Fig. 8) and A4T34 at $I = 16.63$ Ns (Fig. 9). By analysing the images of the test panels, it is clear that the size of the perforation hole is smaller than the diameter of the explosive disk. This reduction in the perforation hole size at high charges cannot be
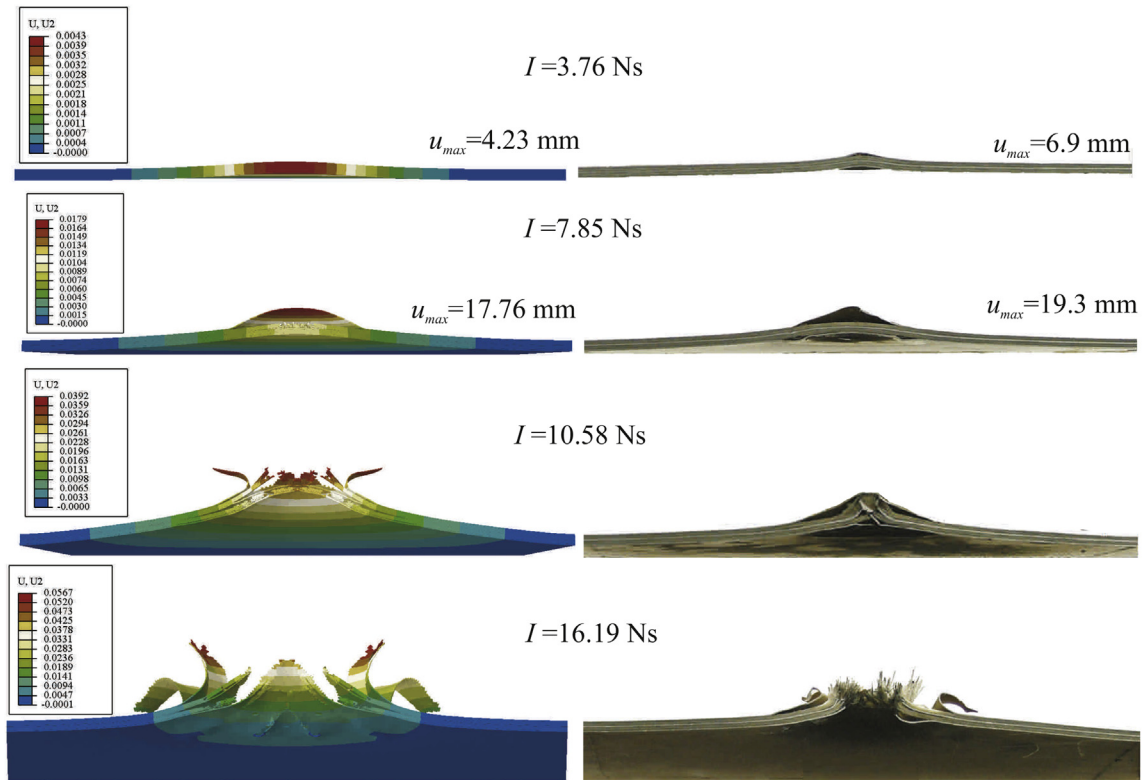
Fig. 8. Comparison of the cross-sections of the deformed FML panel A3T24 over a range of the blast impulses.

reproduced when the spatial distribution of the pressure function in Eq. (15) is assumed to be the same for all the loading cases. In the simulations, the uniform pressure applied in the centre of the panel inevitably causes deformation and crushing of composite and aluminium layers over an area that is equal to the size of explosive disc, which leads to an over-estimation of the failure zone in this region. Previous work on blast failure in sandwich panels 25 suggests that the pressure distribution may be non-uniform over the area of the explosive disk. Altering the spatial distribution of the pressure function was not the objective of the current research,

however, parametric studies with the FML panel models as presented here can be instrumental in determining the loading function parameters that more accurately describe the pressure distribution at high charges.

One of the most distinctive modes of failure in the FMLs, observed in most of the loading cases, was debonding between the layers of composite and metal. A quantitative assessment of this mode of failure was conducted by Lemanski at al. [26], who used an average debonding length to estimate the extent of this failure mode in different loading cases. Specifically, the average debonding
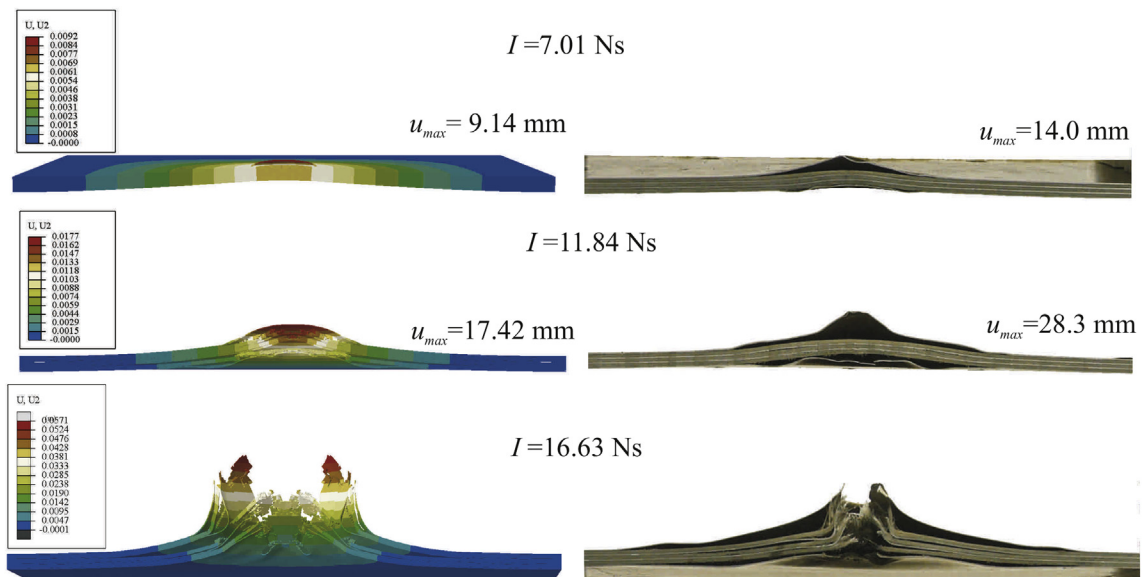

Fig. 9. Comparison of the predicted displacement contour plots with the cross-sections of the deformed FML panel A4T34 [6] over a range of the blast impulses.
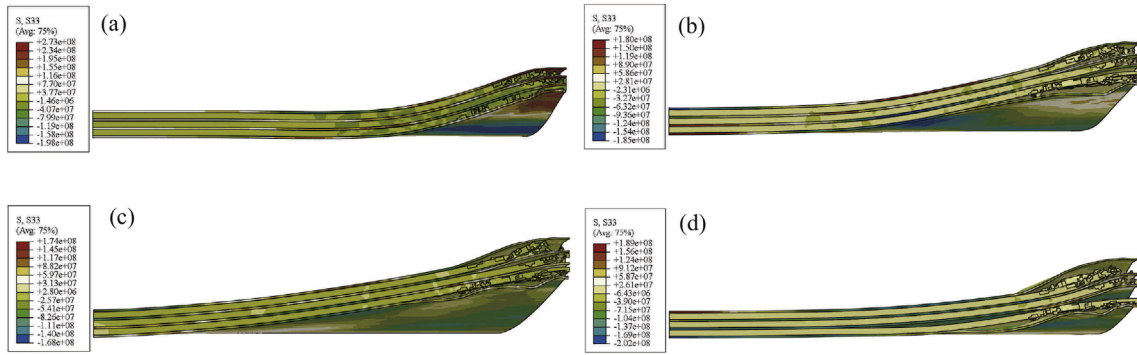
Fig. 10. Transient response of the A4T34 panel at $I = 11.84$ Ns presented as in-plane stress, σ_{22}, contour plots at (a) $t = 0.1$ ms, (b) $t = 0.4$ ms, (c) $t = 0.7$ ms, (d) $t = 1.4$ ms.
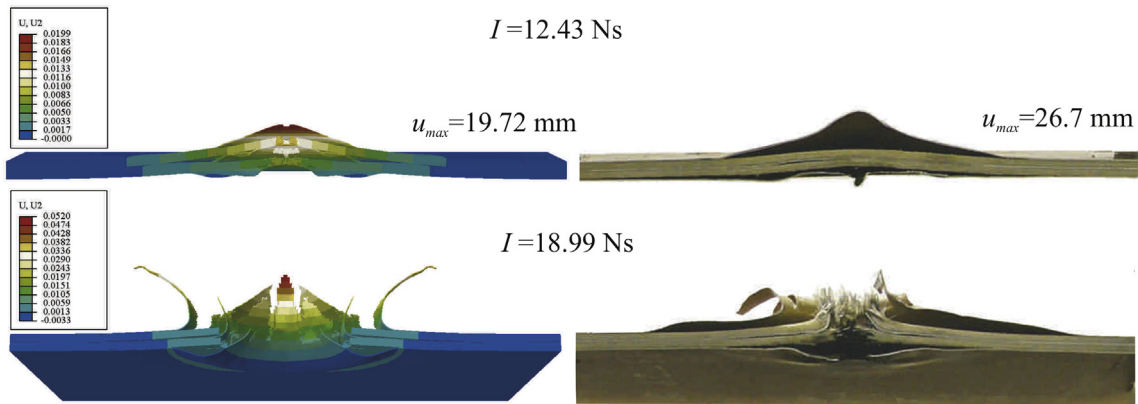

Fig. 11. Comparison of the calculated contour plots with the experimentally observed deformation and failure of FML panel A3T28 [6].

length, l_{avg}, as a percentage of the undeformed plate width, was calculated as follows [6,26].

$$l_{avg} = \frac{1}{N} \sum_{i=1}^{N} \frac{l_i}{L} \times 100\% \qquad (19)$$

where l_i is the length of the debonding at each interface, N is the number interfaces, and L is the width of the undeformed panel. The length of debonding at each interface was measured on the cross-sectional images of the panels, as shown schematically in Fig. 12(a).

The assessment has shown that the average length of the debonding tends to increase with applied impulse in most of the cases. Here, the same trend was reproduced numerically, by measuring the debonding lengths predicted in the simulations, and then calculating l_{avg} using Eq. (19). Comparison of the obtained
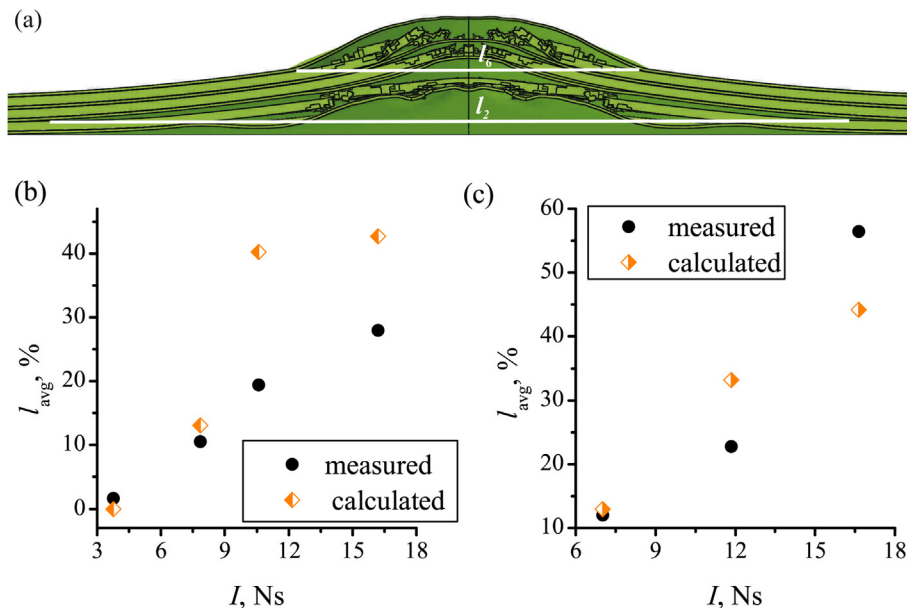

Fig. 12. Measurement of the length of the debonding at metal-composite interfaces (plot (a)) and comparison of the calculated and measured average debonding length in (b) A3T24 FML lay-up and (c) A4T34 FML lay-up.

average length of the debonding with that calculated for the tested panels in Ref. [26] is shown in Fig. 12(b) and (c) for A3T24 FML lay-up and A4T34 FML lay-up, respectively. As can be seen, the calculated data not only reflects the experimental trend of the increase of the average debonding length with the impulse, but there is also a reasonably good agreement, particularly at low values of the impulse.

5. Conclusions

A numerical study on the blast response of FML panels has been presented. Finite element modelling of panels based on various stacking configurations has been carried out using the commercial software package Abaqus/Explicit. Here, a relatively simple continuum mechanics-based material model for the composite has been proposed and implemented into the main program through a user-defined subroutine. The model incorporates 3D constitutive behaviour, a damage evolution law and rate-dependency of the composite material.

Comparisons of the numerical predictions with published experimental data has shown that the model is capable of capturing the observed deformation and damage modes with a good degree of accuracy.

A systematic assessment of the predicted modes of deformation and damage for a variety of the loading cases has been carried out. It has shown that the predictive capability of the models reduces for panels with a larger number of constituent layers. One of the reasons behind this is the conservative criterion for element deletion in composite, resulting in over-estimation of the failure of composite layers, which in turn affects the deformation and damage in the adjacent aluminium and cohesive layers.

In simpler loading cases, however, the predictions from the models are entirely reasonable and accurate. For such cases, the models can be used in their current form to undertake parametric studies that consider varieties of FMLs made with various constituent materials, provided that the choice of the material properties, specifically, the damage-related parameters, is reasonable, so that the blast resistance would not be over-estimated.

Acknowledgements

Appendix

A. Aluminium material model

To model the rate-dependent behaviour of the aluminium layers, Johnson-Cook plasticity and damage initiation criteria, along with the linear evolution of the damage variable with effective plastic displacement, as available in Abaqus [18], were used. When temperature effects are neglected, the appropriate expressions become:

$$\sigma = \left[A + B\left(\bar{\varepsilon}_{pl}\right)^n \right] \left[1 + C \ln\left(\frac{\dot{\bar{\varepsilon}}_{pl}}{\dot{\varepsilon}_0}\right) \right], \tag{A.1}$$

$$\bar{\varepsilon}_D^{pl} = [d_1 + d_2 \exp(d_3 p/q)] \left[1 + d_4 \ln\left(\frac{\dot{\bar{\varepsilon}}_{pl}}{\dot{\varepsilon}_0}\right) \right], \tag{A.2}$$

where σ is the rate-dependent yield stress, $\bar{\varepsilon}_{pl}$ is the equivalent plastic strain, A, B and n are material parameters, C and $\dot{\varepsilon}_0$ are the strain-rate constant and the reference strain rate, respectively. In Eq. (A.2), $\bar{\varepsilon}_D^{pl}$ is the equivalent plastic strain at the onset of damage and d_1 - d_4 are failure parameters. The material properties for the Al2024-O alloy are summarized in Table A.1. Since d_1 - d_4 for Al2024-O are not available in the literature, the values for Al2024-T3 [27] were used instead.

B. Cohesive material model

The constitutive response of the cohesive layers is described in terms of traction versus separation. Damage initiation is defined by a quadratic nominal stress criterion, which is written as follows:

$$\left\{\frac{\langle t_n \rangle}{t_n^0}\right\}^2 + \left\{\frac{t_s}{t_s^0}\right\}^2 + \left\{\frac{t_t}{t_t^0}\right\}^2 = 1, \tag{B.1}$$

where $\langle x \rangle = (|x| + x)/2$ is a Macaulay bracket, t_n, t_s and t_t are the current normal and shear stresses, and t_n^0, t_s^0 and t_t^0 are the peak nominal stresses in the appropriate directions.

Damage evolution is defined via a power law as follows:

$$\left\{\frac{G_n}{G_n^c}\right\} + \left\{\frac{G_s}{G_s^c}\right\} + \left\{\frac{G_t}{G_t^c}\right\} = 1, \tag{B.2}$$

where G_n, G_s and G_t denote the work done by the tractions and their conjugate relative displacements in the normal and the two shear directions, and G_n^c, G_s^c and G_n^t are their associated critical fracture energies. The cohesive interface parameter values are specified in Table B.1. These are similar to the cohesive element material parameters defined in Ref. [28], where the low velocity impact response of composite laminates has been studied. Based on the assessment of the average debonding on the metal-composite interfaces, this is likely to be a conservative estimate of the parameters, since the models tend to overestimate the extent of the debonding at the interfaces. The stiffness and density parameters were scaled to the thickness of the cohesive interface, which in the present study was equal to its geometric thickness.

Table A.1
Material parameters for the aluminium alloy.

Elastic parameters [11]			Johnson-Cook plasticity parameters [17]					Failure constants [27]			
ρ (kg/m³)	E (GPa)	ν	A (MPa)	B (MPa)	n	C	$\dot{\varepsilon}_0$, s^{-1}	d_1	d_2	d_3	d_4
2690	73.1	0.3	76	210	0.4	0.05	1	0.13	0.13	−1.5	0.011

Table B.1
Cohesive layer properties.

General properties			Maximum nominal stresses		Fracture energies	
ρ (kg/m³)	E_n (GPa)	E_s, E_t (GPa)	t_n^0 (MPa)	t_s^0, t_t^0 (MPa)	G_n^c (J/m²)	G_s^c, G_t^c (J/m²)
920	10	4	70	100	300	700

References

[1] L.B. Vogelesang, A. Vlot, Development of fibre metal laminates for advanced aerospace structures, J. Mater. Process Technol. 103 (2000) 1–5.

[2] M. Sadighi, R.C. Alderliesten, R. Benedictus, Impact resistance of fiber-metal laminates: a review, Int. J. Impact Eng. 49 (2013) 77–90.

[3] A. Vlot, Impact loading of fibre metal laminates, Int J Impact Eng 18 (1996) 291–307.

[4] M.R. Abdullah, W.J. Cantwell, The impact resistance of polypropylene-based fibre-metal laminates, Compos Sci. Technol. 66 (2006) 1682–1693.

[5] A. Seyed Yaghoubi, B. Liaw, Effect of lay-up Orientation on ballistic impact behaviors of GLARE 5 FML beams, Int. J. Impact Eng. 54 (2013) 138–148.

[6] G.S. Langdon, G.N. Nurick, S.L. Lemanski, M.C. Simmons, W.J. Cantwell, G.K. Schleyer, Failure characterization of blast-loaded fibre-metal laminate panels based on aluminium and glass-fibre reinforced propylene, Compos. Sci. Technol. 67 (2007) 1385–1405.

[7] G.S. Langdon, S.L. Lemanski, G.N. Nurick, M.C. Simmons, W.J. Cantwell, G.K. Schleyer, Behaviour of fibre-metal laminates subjected to localised blast loading: Part I – experimental observations, Int. J. Impact Eng. 34 (2007) 1202–1222.

[8] G.F.A. Mohamed, C. Soutis, A. Hodzic, Blast resistance and damage modelling of fibre metal laminates to blast loads, Appl. Compos Mater 19 (3–4) (2012) 619–636.

[9] T. Kotzakolios, D.E. Vlachos, V. Kostopoulos, Investigation of blast response of GLARE laminates: comparison against experimental results. Plastics, Rubber Compos. 40 (6–7) (2011) 349–355.

[10] F.D. Morinière, R.C. Alderliesten, R. Benedictus, Modelling of impact damage and dynamics in fibre-metal laminates - a review, Int. J. Impact Eng. 67 (2014) 27–38.

[11] D. Karagiozova, G.S. Langdon, G.N. Nurick, S. Chung Kim Yuen, Simulation of the response of fibre-metal laminates to localised blast loading, Int. J. Impact Eng. 37 (2010) 766–782.

[12] Z. Guan, W.J. Cantwell, R. Abdullah, Numerical modeling of the impact response of fiber-metal laminates, Polym. Compos. 30 (5) (2009) 603–611.

[13] B.A. Gama, J.W. Gillespie Jr., Finite element modeling of impact, damage evolution and penetration of thick-section composites, Int. J. Impact Eng. 38 (2001) 181–197.

[14] C. Soutis, G.F.A. Mohamed, A. Hodzic, Modelling the structural response of GLARE panels to blast load, Appl. Compos Struct. 94 (2011) 267–276.

[15] T.P. Vo, Z.W. Guan, W.J. Cantwell, G.K. Schleyer, Low-impulse blast behavior of fibre metal laminates, Compos Struct. 94 (2012) 954–965.

[16] J.-K. Kim, M.-L. Sham, Impact and delamination failure of woven-fabric composites, Compos Sci. Technol. 60 (5) (2000) 745–761.

[17] E. Sitnikova, Z.W. Guan, G.K. Schleyer, W.J. Cantwell, Modelling of perforation failure in fibre metal laminates subjected to high impulsive blast loading, Int. J. Solids Struct. 51 (18) (2014) 3135–3146.

[18] Abaqus Analysis User's Manual. Abaqus 6.10 HTML Documentation, 2010.

[19] L. Kachanov, Rupture time under creep conditions. Izv Akad Nauk SSSR, Otd. Tekh Nauk. 8 (1958) 26–31 (in Russian).

[20] Z. Hashin, Failure criteria for unidirectional fiber composites, J. Appl. Mech. – T ASME 47 (1980) 329–334.

[21] K.A. Brown, R. Brooks, N.A. Warrior, Numerical simulation of damage in thermoplastic composite materials, in: Proceedings of 5th European LS-dyna Users Conference, 2005.

[22] K.A. Brown, R. Brooks, N.A. Warrior, The static and high strain rate behaviour of a commingled E-glass/polypropylene woven fabric composite, Compos Sci. Technol. 70 (2010) 272–283.

[23] C.A. Weeks, C.T. Sun, Modeling non-linear rate-dependent behavior in fiber-reinforced composites, Compos Sci. Technol. 58 (3–4) (1998) 603–611.

[24] L. Iannucci, Progressive failure modelling of woven carbon composite under impact, Int. J. Impact Eng. 32 (2006) 1013–1043.

[25] G.S. Langdon, D. Karagiozova, C.J. von Klemperer, G.N. Nurick, A. Ozinsky, E.G. Pickering, The air-blast response of sandwich panels with composite face sheets and polymer foam cores: experiments and predictions, Int. J. Impact Eng. 54 (2013) 64–82.

[26] S.L. Lemanski, G.N. Nurick, G.S. Langdon, M.C. Simmons, W.J. Cantwell, G.K. Schleyer, Behaviour of fibre metal laminates subjected to localised blast loading – Part II: quantitative analysis, Int. J. Impact Eng. 34 (2007) 1223–1245.

[27] D.R. Lesuer, Experimental Investigations of Material Models for Ti-6Al-4V Titanium and 2024-T3 Aluminum. Tech Rep, Lawrence Livermore National Laboratory, Livermore, CA, 2000.

[28] Y. Shi, T. Swait, C. Soutis, Modelling damage evolution in composite laminates subjected to low velocity impact, Compos Struct. 94 (2012) 2902–2913.